Building time-lapse VTI models from coupled fluid-geomechanical simulation

Yinbin Ma, Mark A. Meadows, and Biondo Biondi

ABSTRACT

A synthetic time-lapse (4D) model with changes that closely match those from a producing reservoir would improve our understanding of the 4D seismic data. In this paper we present a workflow to build a time-lapse vertical transversely isotropic (VTI) model based on coupled fluid-geomechanical simulation data.

INTRODUCTION

Full waveform inversion (FWI) estimates high-resolution subsurface models by minimizing the mismatch between the observed seismic data and synthetic data (Tarantola, 1984; Virieux and Operto, 2009). FWI is a useful tool for 4D seismic imaging problems (Denli and Huang, 2009; Routh et al., 2012; Maharramov and Biondi, 2014). However, 4D FWI faces the challenge of detectability from the seismic surveys, particularly for the estimation of anisotropic parameters.

In this paper, we present a workflow to build a synthetic time-lapse VTI model to help us understand the feasibility of estimating anisotropic parameters and improve 4D FWI strategies. The synthetic model is built based on a coupled flow and geomechanical simulation of a producing reservoir, and has been calibrated based on the fields pressure history during production. Our synthetic model has been designed to contain time-lapse changes that are close to those arising from production effects observed in the field data.

The paper is organized as follows. In the METHOD section, we show the workflow to build the synthetic time-lapse model. Next, we give an overview of the geomechanical model. In the following sections, we explain the workflow to build the baseline and monitor models in detail. We test the synthetic model with seismic imaging in the last section.

METHOD

We build a synthetic time-lapse seismic VTI model with output from a coupled flow and geomechanical simulation in an isotropic medium. The static Youngs modulus (E), static Poissons ratio (ν), density, stress and strain from the geomechanical model are required to build the VTI model.

To convert the geomechanical model to the seismic model, we designed the following workflow:

1. Extract static E and ν from geomechanical model
2. Convert static properties to dynamic E and ν
3. Compute dynamic Vp and Vs by adjusting the dynamic-to-static ratio in step 2 based on the field model used previously for seismic migration
4. Add constant ε and reasonable δ based on the field model, to get the baseline VTI model
5. Compute the strain and stress for the baseline and monitor models by coupled flow-geomechanical simulation
6. Use third-order elasticity to estimate stiffness tensor changes in a tilted reference frame represented by the triaxial components of stress (orientation determined by the stress and strain outputs)
7. Rotate the change in stiffness tensor back to the field model reference frame
8. Project the monitor stiffness tensor changes to the closest VTI model (Dellinger, 2005). Adjust coefficients for third-order elasticity by repeating steps 6-8 until the seismic time-lapse change matches the value observed from the field.

At the end of the workflow, we have a time-lapse seismic VTI model in finite-element cells. It is straightforward to convert the finite element model to finite difference model (see Appendix)

In the following sections, we will illustrate each step in the workflow with a numerical example from the Genesis Field.

OVERVIEW OF THE GOEMECHANICAL MODEL

In this paper, we explain and demonstrate our workflow using the geomechanical model from the Genesis Field (Magesan et al., 2005; Hodgson et al., 2007). The geomechanical model has 330174 cells with 83 shale and sand layers. The coupled flow-geomechanical simulation is conducted with Stanfords AD-GPRS package. Over the same field, a velocity model constructed from the seismic data was previously

constructed. In Figure 1, we show the coverage of the geomechanical model and seismic model. The major axes of the two models are rotated 18.3° with respect to each other.

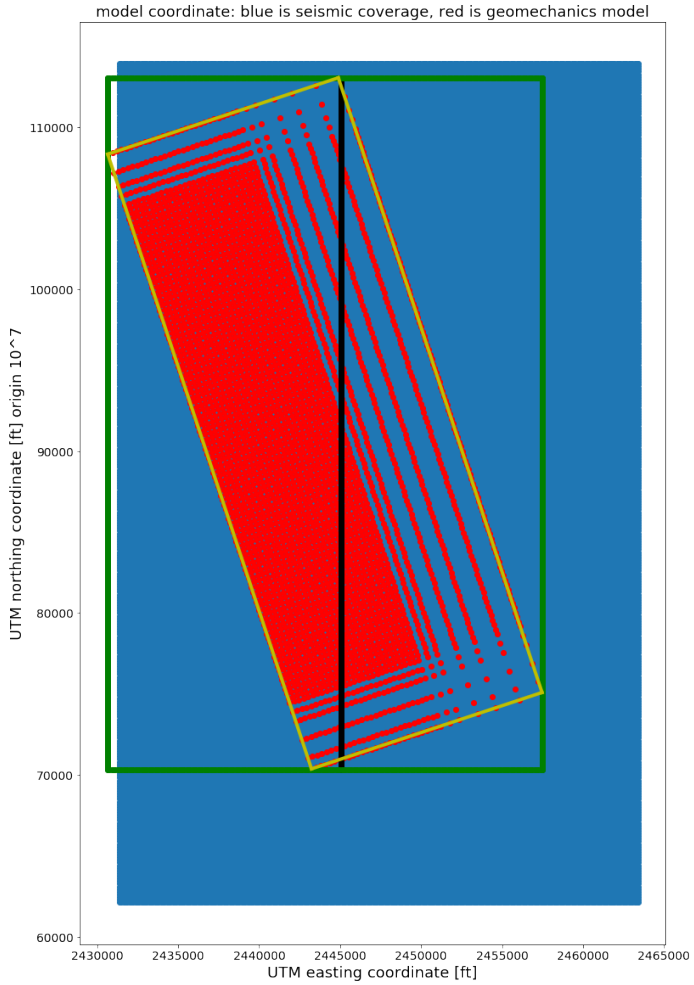

Figure 1: A depth slice of the coverage from the geomechanical and seismic models. Red dots are the vertices of the geomechanical model. Blue area represents the coverage of the seismic velocity model. The black line is the location of the 2D models displayed in the following sections. Green and yellow rectangles represent the coverage of 2 synthetic models we built with our workflow (to align with the seismic and geomechanical models, respectively). [**CR**]

BUILDING A VTI BASELINE MODEL

We first extract static Young's modulus $\mathbf{E}_{\text{static}}$, static Poisson's ratio ν_{static} and the density ρ from the geomechanical model.

We need dynamic properties to estimate the stiffness tensor and acoustic velocity. We convert $\mathbf{E}_{\text{static}}$, ν_{static} to $\mathbf{E}_{\text{dynamic}}$, ν_{dynamic} based on typical values of the static-to-

dynamic ratio from the field, tuned to approximate the migration velocities from this area. In Figure 2, we show dynamic Youngs modulus, dynamic Poissons ratio and the density.

With the dynamic elastic properties, we build the stiffness tensor for isotropic media,

$$\begin{bmatrix} C_{11} & C_{12} & C_{12} & 0 & 0 & 0 \\ C_{12} & C_{11} & C_{12} & 0 & 0 & 0 \\ C_{12} & C_{12} & C_{11} & 0 & 0 & 0 \\ 0 & 0 & 0 & C_{44} & 0 & 0 \\ 0 & 0 & 0 & 0 & C_{44} & 0 \\ 0 & 0 & 0 & 0 & 0 & C_{44} \end{bmatrix}, \tag{1}$$

with the following equations:

$$C_{11} = \frac{E(1-\nu)}{(1+\nu)(1-2\nu)} = \lambda + 2\mu \tag{2}$$

$$C_{12} = \frac{E\nu}{(1+\nu)(1-2\nu)} = \lambda \tag{3}$$

$$C_{44} = \frac{E}{2(1+\nu)} = \mu, \tag{4}$$

where E and ν are the dynamic Young's modulus and Poisson's ratio respectively.

The isotropic P- and S-wave velocities (shown in Figure 3) are computed with,

$$Vp = \sqrt{\frac{C_{11}}{\rho}} \tag{5}$$

$$Vs = \sqrt{\frac{C_{44}}{\rho}}. \tag{6}$$

We need a VTI baseline model with the corresponding stiffness tensor,

$$\begin{bmatrix} C_{11} & C_{12} & C_{13} & 0 & 0 & 0 \\ C_{12} & C_{11} & C_{13} & 0 & 0 & 0 \\ C_{13} & C_{13} & C_{33} & 0 & 0 & 0 \\ 0 & 0 & 0 & C_{44} & 0 & 0 \\ 0 & 0 & 0 & 0 & C_{44} & 0 \\ 0 & 0 & 0 & 0 & 0 & C_{66} \end{bmatrix}, \tag{7}$$

with 5 independent parameters, which means that we need to add 3 independent parameters manually to the previous isotropic model.

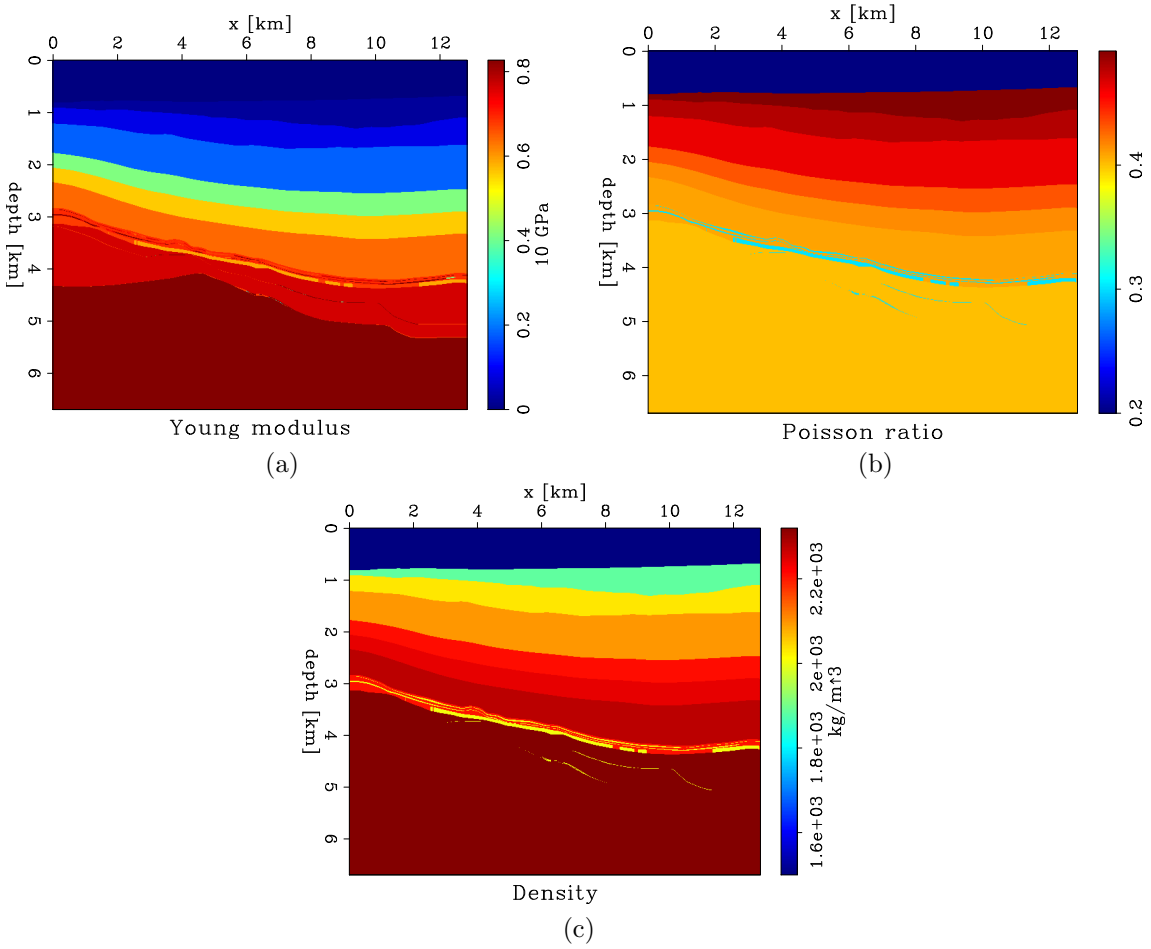

Figure 2: Isotropic elastic parameters [**CR**]

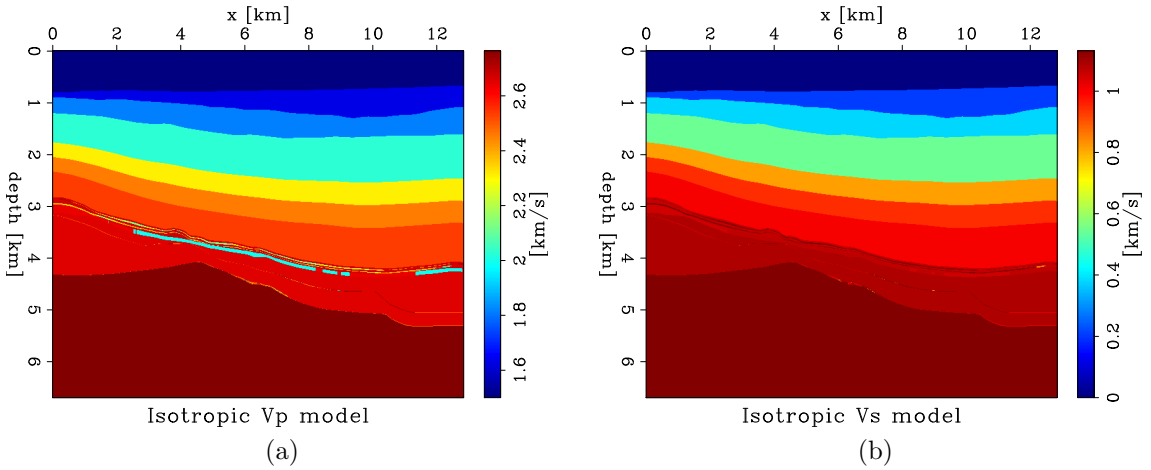

Figure 3: Isotropic velocity model [**CR**]

The relation between the VTI model and the stiffness tensor is:

$$\varepsilon = \frac{C_{11} - C_{33}}{2C_{33}} = \frac{V_h^2 - V_z^2}{2V_z^2} \tag{8}$$

$$\delta = \frac{(C_{13} + C_{44})^2 - (C_{33} - C_{44})^2}{2C_{33}(C_{33} - C_{44})} = 0.5\left(\frac{V_{nmo}^2}{V_z^2} - 1\right) \tag{9}$$

$$\gamma = \frac{C_{66} - C_{44}}{2C_{44}} \tag{10}$$

$$\eta = \frac{\varepsilon - \delta}{1 + 2\delta} = 0.5\left(\frac{V_h^2}{V_{nmo}^2} - 1\right). \tag{11}$$

In this paper, we ignore γ because it controls shear wave anisotropy, which means that $C_{44} = C_{66}$. For the other 3 anisotropic parameters ε, δ and η, only 2 are independent. We add $\varepsilon = 0.17$, based on our knowledge that V_h/V_z has value between 1.1 and 1.2. We use η with a value close to what we observe from the field data.

Introducing ε will modify either C_{11} or C_{33}. We choose to increase C_{11} and use isotropic V_p as V_z. Introducing δ will change C_{13} or C_{44}. We fix C_{44} and modify C_{13} assuming that the model is isotropic for shear velocity.

In Figure 4, we show the ε, δ, η and the corresponding V_z model for the baseline.

TIME-LAPSE CHANGE OF THE VTI MODEL

We extract the 6-component stress and strain tensors in Voigt notation from the geomechanical simulation. The elastic strain and stress satisfy the following equation,

$$\sigma_i = C_{ij}\varepsilon_j, \tag{12}$$

where σ_i is the stress, C_{ij} is the stiffness tensor and ε_j is the elastic strain. We will use both Voigt notation and the tensor form for the rest of the paper. Conversion between different notations is trivial and summarized in the Appendix in the section on Notations on strain, stress and stiffness tensor.

In Figure 5 we show the change in vertical strain and volumetric strain after simulating of $\sim$ 1200 days. We observe a reservoir compaction which leads to an increase in both vertical strain and volumetric strain. The overburden dilation leads to a decrease in vertical strain and stress, while volumetric strain remain unchanged.

We use the third-order elasticity equations (Herwanger and Horne, 2009) to estimate the change in the stiffness tensor. Assuming a reference stiffness tensor C_{ij}^0, we can compute the stiffness tensor C_{ij}' in a triaxial stress state reference frame using Voigt notation,

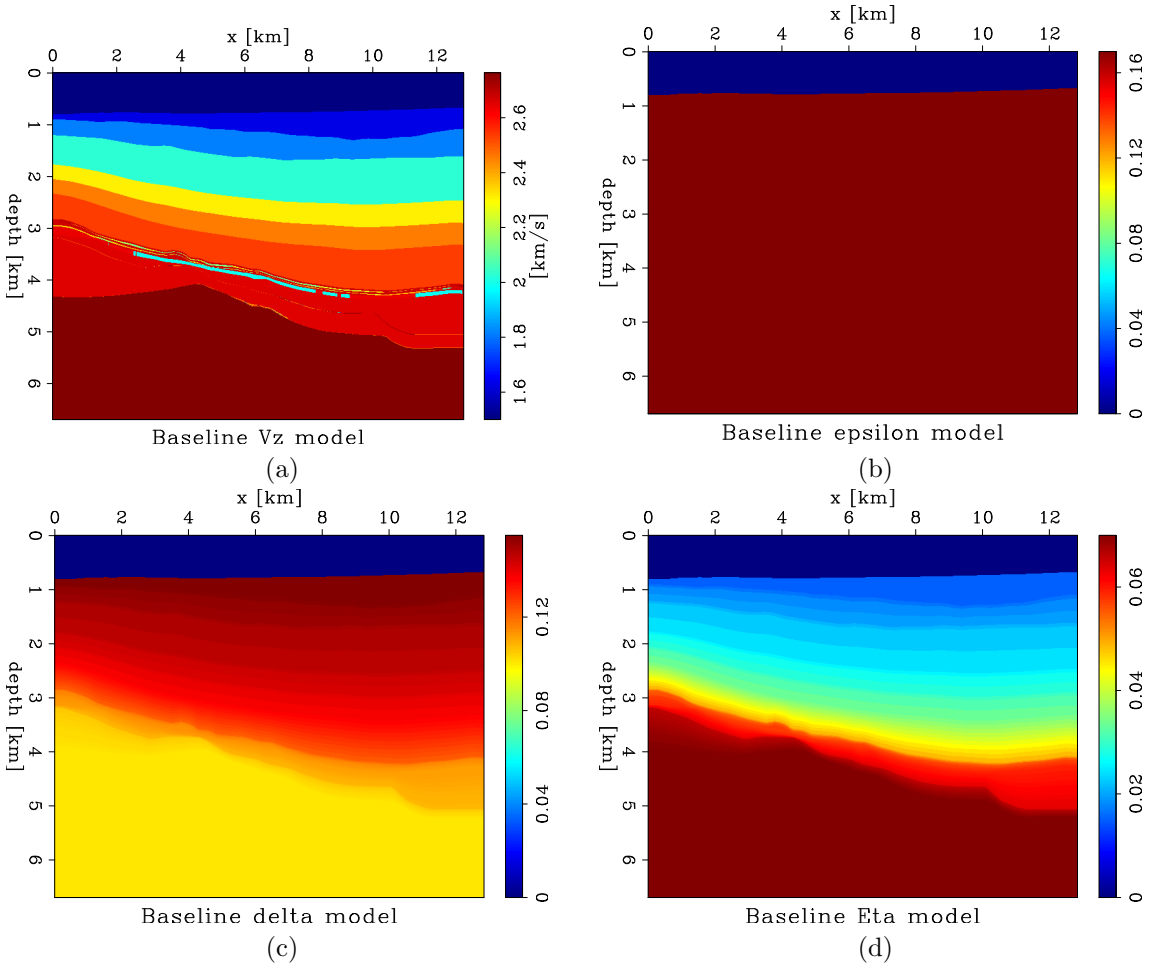

Figure 4: (a) constant ε model. (b) δ model. (c) Vertical velocity. [**CR**]

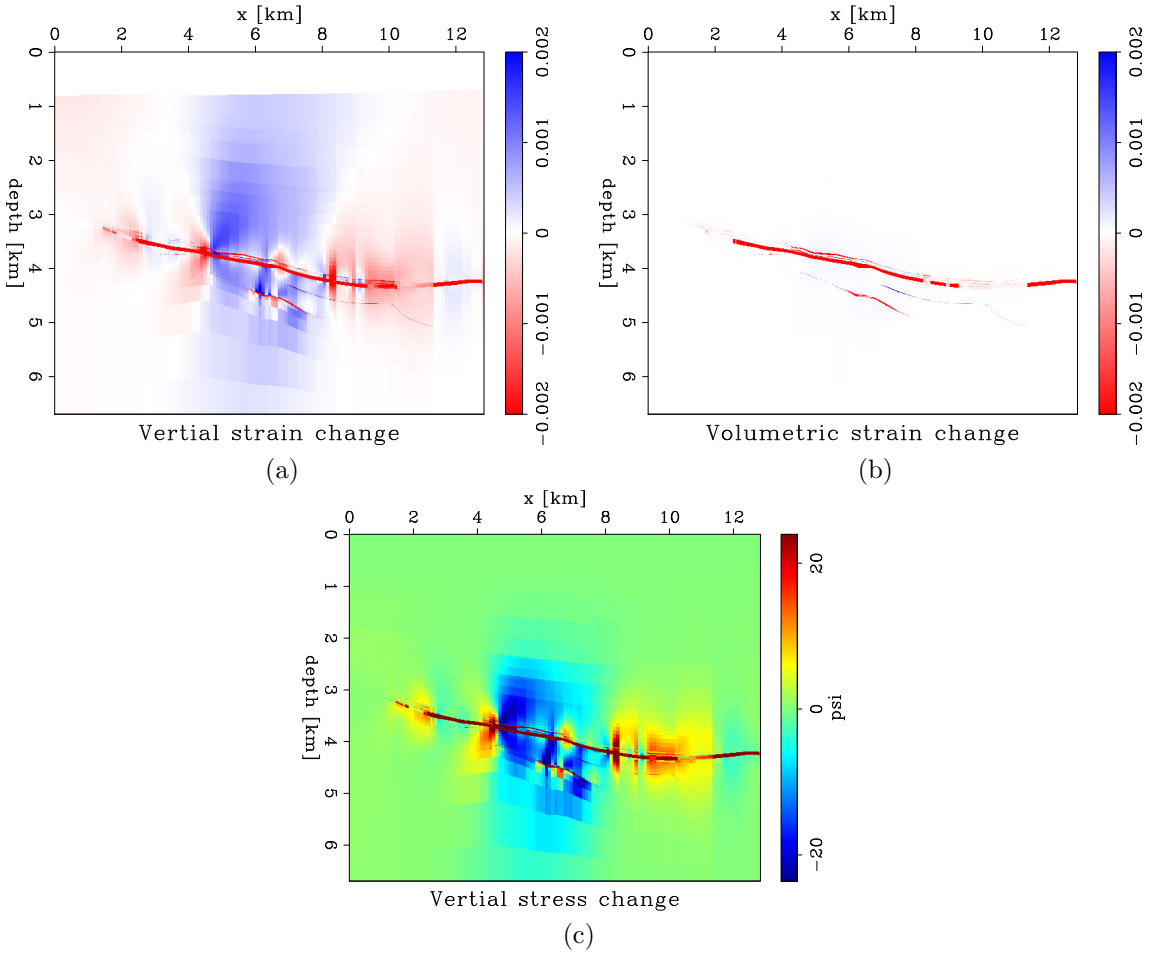

Figure 5: (a) Vertical strain change after production for $\sim$ 1200 days. (b) volumetric strain change. (c) Vertical stress change. [**CR**]

$$
\begin{aligned}
C'_{11} &\approx C^0_{11} + c_{111}\varepsilon'_{11} + c_{112}(\varepsilon'_{22} + \varepsilon'_{33}) \\
C'_{22} &\approx C^0_{22} + c_{111}\varepsilon'_{22} + c_{112}(\varepsilon'_{11} + \varepsilon'_{33}) \\
C'_{33} &\approx C^0_{33} + c_{111}\varepsilon'_{33} + c_{112}(\varepsilon'_{11} + \varepsilon'_{22}) \\
C'_{12} &\approx C^0_{23} + c_{112}(\varepsilon'_{11} + \varepsilon'_{22}) + c_{123}\varepsilon'_{33} \\
C'_{13} &\approx C^0_{23} + c_{112}(\varepsilon'_{11} + \varepsilon'_{33}) + c_{123}\varepsilon'_{22} \\
C'_{23} &\approx C^0_{23} + c_{112}(\varepsilon'_{22} + \varepsilon'_{33}) + c_{123}\varepsilon'_{11} \\
C'_{66} &\approx C^0_{66} + c_{144}\varepsilon'_{33} + c_{155}(\varepsilon'_{11} + \varepsilon'_{22}) \\
C'_{55} &\approx C^0_{55} + c_{144}\varepsilon'_{22} + c_{155}(\varepsilon'_{11} + \varepsilon'_{33}) \\
C'_{44} &\approx C^0_{44} + c_{144}\varepsilon'_{11} + c_{155}(\varepsilon'_{22} + \varepsilon'_{33}),
\end{aligned} \tag{13}
$$

where we have five stress-sensitivity coefficients c_{ijk} (although only three are independent). The prime $'$ denote properties in the rotated triaxial reference determined by the stress $\sigma'_{mn} = R_{mi}R_{nj}\sigma_{ij}$, where σ'_{mn} is a diagonal matrix and R_{mi} is the rotation matrix.

While equation 13 has compact form, it is inconvenient to compute numerically, due to the complexity of axis rotation under Voigt notation. We rewrite the third-order elasticity equations 13 as

$$\Delta C'_{abcd} = T'_{abcdef}\varepsilon'_{ef}, \tag{14}$$

where T'_{abcdef} is a sixth-order tensor with coefficients determined by c_{ijk} (we do not explicitly list T'_{abcdef} here). With equation 14, our model becomes orthorhombic in the rotated triaxial reference frame.

Equation 14 is valid in the rotated frame with orientation determined by the stress. We know the value of ε model in the reference frame (x-y-z), as well as T'_{abcdef} in the rotated frame, and we would ultimately like to compute C_{ijkl} for the monitor model in the model reference frame.

There are two different approaches to compute C_{ijkl}. In the first approach, we can rotate ε_{ij} to the triaxial stress direction ε'_{ef}, compute $\Delta C'_{abcd}$ and rotate it back to model reference frame to get ΔC_{ijkl}:

$$
\begin{aligned}
\varepsilon'_{ef} &= R_{em}R_{fn}\varepsilon_{mn} \\
\Delta C'_{abcd} &= T'_{abcdef}\varepsilon'_{ef} \\
\Delta C_{ijkl} &= R_{ai}R_{bj}R_{ck}R_{dl}\Delta C'_{abcd}.
\end{aligned} \tag{15}
$$

In the second approach, we rotate the tensor T'_{ijklmn} to the reference frame, and then directly estimate ΔC_{abcd} from ε_{ab}:

$$
\begin{aligned}
T_{ijklmn} &= R_{ai}R_{bj}R_{ck}R_{dl}R_{em}R_{fn}T'_{abcdef} \\
\Delta C_{ijkl} &= T_{ijklmn}\varepsilon_{mn}.
\end{aligned} \tag{16}
$$

We implement both equation 15 and 16 and verify that the outputs are the same up to machine precision (10^{-16}). Mathematically they are exactly the same, we compare the results to find potential problems in our implementation.

Once we get the change in stiffness tensor, we can compute the monitor model as,

$$C_{ijkl}^{\text{mon}} = C_{ijkl}^{\text{base}} + \Delta C_{ijkl}, \tag{17}$$

where C_{ijkl}^{mon} is the sum of the VTI stiffness tensor C_{ijkl}^{base}, and a tilted orthorhombic stiffness tensor ΔC_{ijkl}.

C_{ijkl}^{mon} is then into a model that we can use currently, we need to project it to the nearest VTI model using the $\mathbf{L}_2$ norm distance,

$$\|C^{\text{mon}} - C^{\text{mon,VTI}}\| \rightarrow \min \tag{18}$$

Stiffness tensor projection to a VTI model using equation 18 is straightforward using tensor notation. In the Appendix section on **Notations on strain, stress and stiffness tensor**, we derive the formula to solve equation 18 under Voigt notation.

From the stiffness tensor $C^{\text{mon,VTI}}$, we can derive the monitor VTI model using equation (2), as well as the corresponding time-lapse change based on the baseline model we built earlier.

In Figure 6, we show the time-lapse change for V_z, ϵ, δ and η. In the reservoir area, we observe an increase in V_z and a decrease in anisotropic parameters (ϵ, δ), due to reservoir compaction. In the overburden area, we observe a slowdown in V_z and an increase in anisotropy (ϵ, δ), consistent with the previous study (Herwanger and Horne, 2009). η decreases in the overburden because the shale layers become more "isotropic" as a consequence of stress unloading.

So far, we have shown the workflow to estimate a time-lapse change in the VTI model. It is also important to understand how the changes depend on the strain, stress and stiffness tensors. We only consider the first-order changes of VTI parameters with respect to the stiffness tensor, as follows,

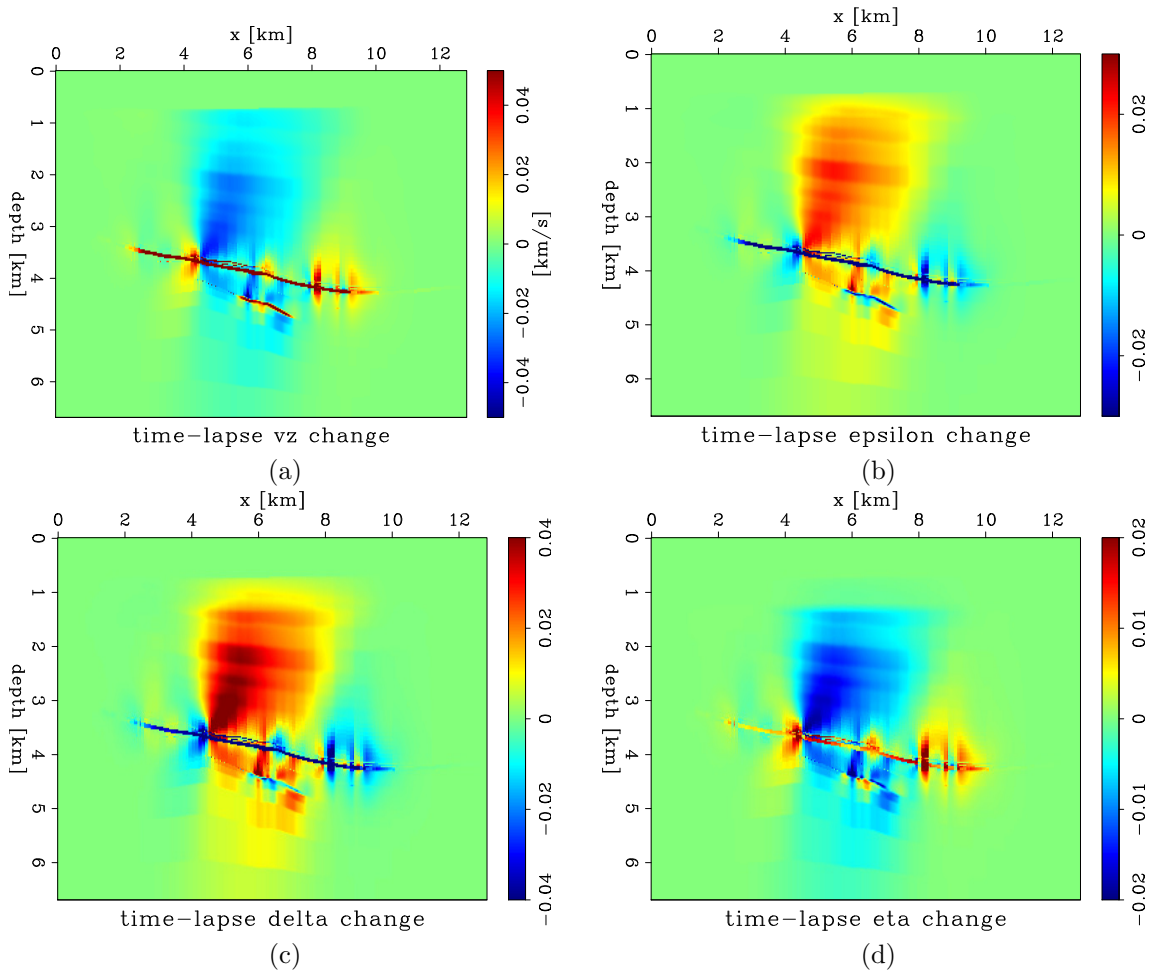

Figure 6: (a) time-lapse Vz change; (b) time-lapse ϵ change; (c) time-lapse δ change; (c) time-lapse η change. [**CR**]

$$\Delta V_z^2 = \frac{1}{\rho}\Delta C_{33} - \frac{C_{33}}{\rho}\Delta\rho \tag{19}$$

$$\Delta V_{nmo}^2 = \frac{1}{\rho}\Delta C_{11} - \frac{C_{11}}{\rho}\Delta\rho \tag{20}$$

$$\Delta\varepsilon = \frac{1}{2C_{33}}\Delta C_{11} - \frac{C_{11}}{2C_{33}^2}\Delta C_{33} \tag{21}$$

$$\Delta\delta = \frac{C_{13}+C_{44}}{C_{33}\left(C_{33}-C_{44}\right)}\Delta C_{13} + \frac{\left(C_{13}+C_{33}\right)^2}{2C_{33}\left(C_{33}-C_{44}\right)^2}\Delta C_{44} \tag{22}$$

$$+ \frac{-C_{33}^2C_{44} + C_{13}^2\left(-2C_{33}+C_{44}\right) + 2C_{13}C_{44}(-2C_{33}+C_{44})}{2C_{33}^2\left(C_{33}-C_{44}\right)^2}\Delta C_{33} \tag{23}$$

$$\Delta\eta = \frac{C_{13}+C_{44}}{C_{33}\left(C_{33}-C_{44}\right)}\Delta C_{13} - \frac{C_{11}\left(C_{13}+C_{33}\right)^2}{2\left(C_{13}^2+2C_{13}C_{44}+C_{33}C_{44}\right)^2}\Delta C_{44} \tag{24}$$

$$+ \frac{C_{11}\left(C_{13}+C_{44}\right)^2}{2\left(C_{13}^2+2C_{13}C_{44}+C_{33}C_{44}\right)^2}\Delta C_{33} \tag{25}$$

PRELIMINARY SEISMIC IMAGING STUDY BASED ON THE SYNTHETIC MODEL

With the synthetic model we built in the previous part of the paper, we test the sensitivity of the time-lapse seismic data with respect to different parameters in the VTI model. (The time-lapse VTI model used here is slightly different from the one we constructed earlier in the paper, as explained below.)

Time-lapse velocity change

For the first numerical experiment, we migrate the baseline data and monitor data with the same baseline VTI model. We use towed-streamer acquisition with offsets up to 5 km.

As we have a time-lapse velocity decrease in the overburden, we may expect the monitor image to be less coherent compared to the baseline image, as shown in Figure 7. The baseline and monitor images do not register in depth, as expected. The angle gathers near the production area are shown in Figure 8, where we see a clear curvature change in the monitor data, which is an indication of the production-induced velocity change.

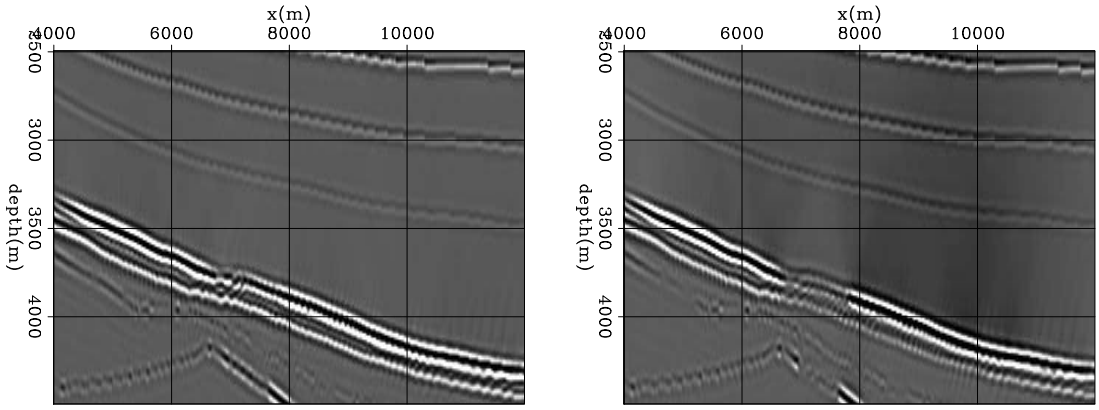

Figure 7: Migration of baseline (left) and monitor (right) data. We migrate both data with the baseline VTI model. [**CR**]

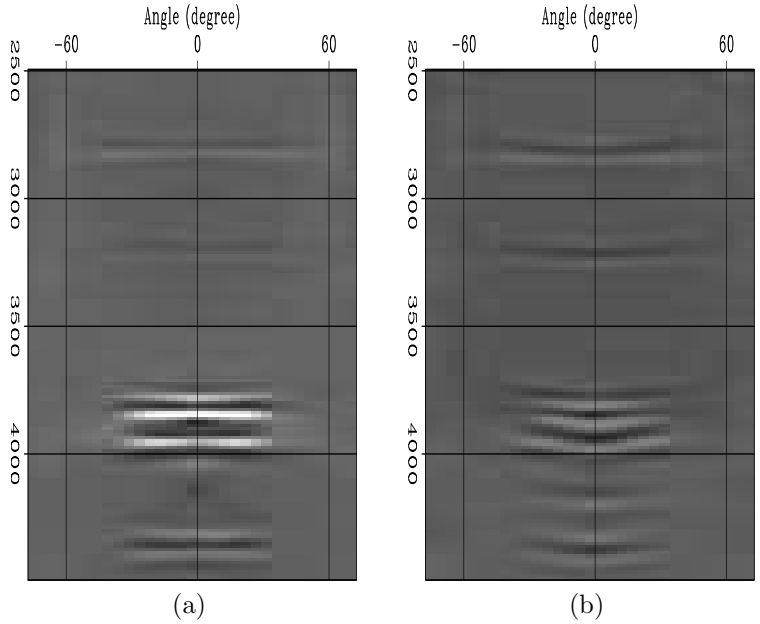

Figure 8: ADCIG for baseline(left) and monitor (right) data, with offset up to 5 km. [**CR**]

Time-lapse anisotropic parameter change

Estimation of the production-induced change in anisotropic parameters is challenging due to the fact that these parameters have a second-order effect on the seismic data for limited offset-to-depth ratios.

To illustrate this point, we perform the following numerical test. The baseline data are migrated with the correct VTI model. The monitor data are migrated with the correct v_z and v_{nmo}, but incorrect η. Assuming that we do not know the time-lapse change in η(or horizontal velocity); consequently, we use the same value from the baseline model to migrate the monitor data. The estimation of horizontal velocity requires long offsets, which may not be feasible for towed-streamer acquisitions with relatively small offset-to-depth ratios, as in this case with a reservoir depth of 3500m below sea level and a maximum offset of 5 km.

The migrated images with offsets up to 5 km are shown in Figure 9, and angle gathers are shown in Figure 10. With limited offsets, we do not see observable curvature changes in the angle gathers.

In the event that we do have longer offsets, we start to see the effect of η in the angle gathers, as shown in Figure 11.

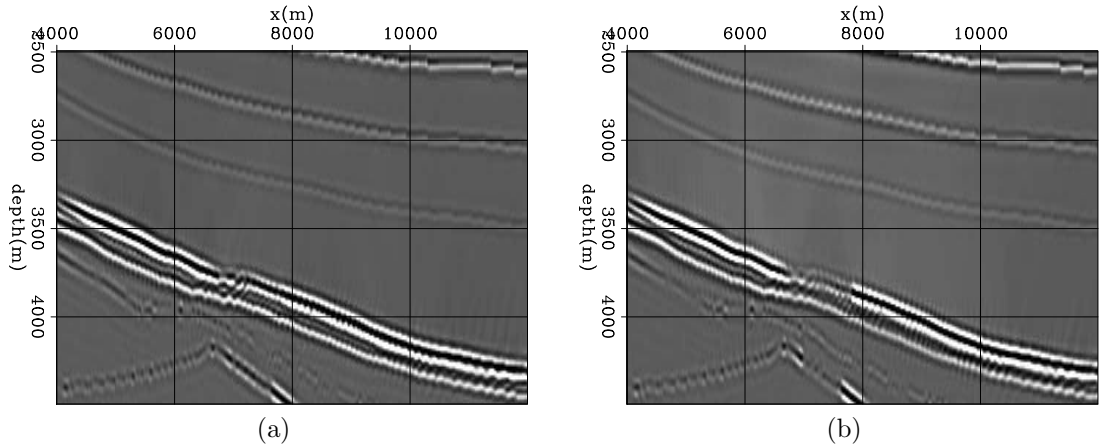

(a) (b)

Figure 9: Migration of baseline (left) and monitor (right) data. Both are migrated with the correct v_{nmo} and v_z. We assume the v_h for monitor model is unknown. [**CR**]

CONCLUSIONS

In this paper, we presented a workflow to build a synthetic time-lapse VTI model from coupled flow and geomechanical simulation data. The modeled time-lapse changes are similar to those observed in the real data and include reservoir compaction and overburden dilation effects. We perform initial seismic imaging tests based on the synthetic model, suggesting the necessity to use long offsets for estimating the time-lapse change in anisotropic parameters.

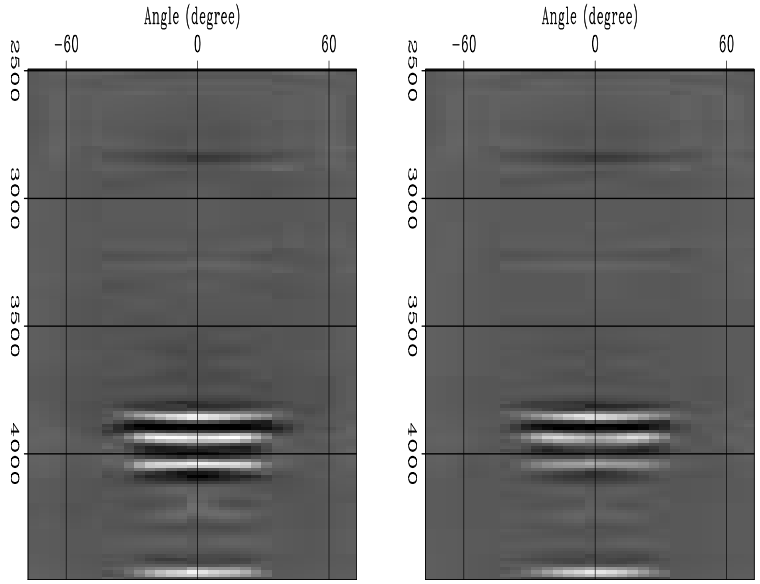

(a) (b)

Figure 10: ADCIG for baseline(left) and monitor (right) data, with offset up to 5 km. Both are migrated with the correct v_{nmo} and v_z. We assume the v_h for monitor model is unknown. [**CR**]

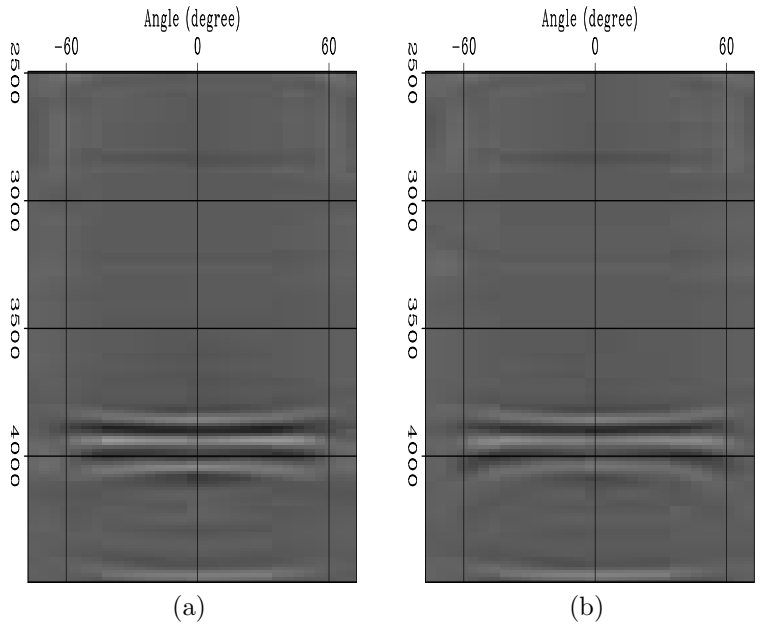

(a) (b)

Figure 11: ADCIG for baseline(left) and monitor (right) data, with offset up to 5 km. Both are migrated with the correct v_{nmo} and v_z. We assume the v_h for monitor model is unknown. [**CR**]

ACKNOWLEDGMENTS

The authors would like to thank the sponsors of the Stanford Exploration Project for their support. We would like to thank Timur Garipov for the support on ADGPRS and geomechanical simulation.

APPENDIX

Conversion between finite-difference model and finite-element model

The conversion between the finite-element model (FEM)and finite-difference model (FDM) is straight- forward, but can be time consuming if not designed carefully.

For the 3D synthetic model we created, we have $\sim 10^9$ grid points. For each point in our finite difference model, we need to find the finite-element cells that contain it.

To accelerate the model conversion, we used the following algorithm. We register the finite-element cells to the finite-difference grid points, and save it to a dictionary. The dictionary initially takes hours to build . Once we build the dictionary, each model conversion takes a few seconds to build a 3D model with a grid-point size of 10^9.

Algorithm 1 model conversion between FDM and FEM

1: initialize mapping function P2C, C2P (P2C maps the finite-different model index to the finite-element cell index) each cell $C_{FEM}(j)$, j= 1,$\cdots$,M
2: find vertices $S_j = \{v_{j,1}, \cdots, v_{j,k}\}$ for $C_{FEM}(j)$
3: build the convex hull $Conv(S_j)$
4: find grid-point candidates P_{cand} near $Conv(S_j)$ each point p in P_{cand} p is in the interior of $Conv(S_j)$
5: find index i for point p in the finite-difference grid
6: $P2C(i) = j$
7: $C2P(j) = i$ each grid point $P_{FD}(i)$, i =1,$\cdots$, N
8: $\text{Model}_{FDM}(P_{FDM}(i)) = \text{Model}_{FEM}(C_{FEM}(P2C(i))$

Notations on strain, stress and the stiffness tensor

Voigt notation is a method to represent a symmetric tensor. For the theory of elasticity, we have the following connections between Voigt notation and the tensor form for stress:

$$(\sigma_{11}, \sigma_{22}, \sigma_{33}, \sigma_{23}, \sigma_{13}, \sigma_{12}) = (\sigma_1, \sigma_2, \sigma_3, \sigma_3, \sigma_4, \sigma_5, \sigma_6) \tag{26}$$

and for strain,

$$(\varepsilon_{11}, \varepsilon_{22}, \varepsilon_{33}, 2\varepsilon_{23}, 2\varepsilon_{13}, 2\varepsilon_{12}) = (\varepsilon_1, \varepsilon_2, \varepsilon_3, \varepsilon_3, \varepsilon_4, \varepsilon_5, \varepsilon_6) \tag{27}$$

A factor of 2 appears in the expression for strain in order that free energy is conserved under both notations:

$$F = \sigma_{ij}\varepsilon_{ij} = \sigma_i\varepsilon_i \tag{28}$$

For the stiffness tensor, we have the representation $C_{ij}, i, j = 1, 2, 3, 4, 5, 6$ in Voigt notation, and $C_{ijkl}, i, j, k, l = 1, 2, 3$ under symmetric tensor representation. To estimate the distance between two stiffness tensor, we need to adjust the coefficients when using the Voigt notation:

$$\begin{aligned}
\|C^A - C^B\|_2^2 &= \sum_{ijkl} \left(C^A_{ijkl} - C^B_{ijkl}\right)^2 && (29)\\
&= (C^A_{11} - C^B_{11})^2 + (C^A_{22} - C^B_{22})^2 + (C^A_{33} - C^B_{33})^2 && (30)\\
&\quad +2 \times \left[(C^A_{12} - C^B_{12})^2 + (C^A_{13} - C^B_{13})^2 + (C^A_{23} - C^B_{23})^2\right] && (31)\\
&\quad +4 \times \left[(C^A_{44} - C^B_{44})^2 + (C^A_{55} - C^B_{55})^2 + (C^A_{66} - C^B_{66})^2\right] && (32)\\
&\quad +4 \times \left[(C^A_{14} - C^B_{14})^2 + (C^A_{15} - C^B_{15})^2 + (C^A_{16} - C^B_{16})^2\right] && (33)\\
&\quad +4 \times \left[(C^A_{24} - C^B_{24})^2 + (C^A_{25} - C^B_{25})^2 + (C^A_{26} - C^B_{26})^2\right] && (34)\\
&\quad +4 \times \left[(C^A_{34} - C^B_{34})^2 + (C^A_{35} - C^B_{35})^2 + (C^A_{36} - C^B_{36})^2\right] && (35)\\
&\quad +8 \times \left[(C^A_{45} - C^B_{45})^2 + (C^A_{46} - C^B_{46})^2 + (C^A_{56} - C^B_{56})^2\right] && (36)
\end{aligned}$$

In general, the tensor form is more intuitive in terms of distance, and rotation angle.

REFERENCES

Dellinger, J., 2005, Computing the optimal transversely isotropic approximation of a general elastic tensor: GEOPHYSICS, **70**, I1–I10.

Denli, H., and L. Huang, 2009, *in* Doubledifference elastic waveform tomography in the time domain: 2302–2306.

Herwanger, J. V., and S. A. Horne, 2009, Linking reservoir geomechanics and time-lapse seismics: Predicting anisotropic velocity changes and seismic attributes: GEOPHYSICS, **74**, W13–W33.

Hodgson, N., C. MacBeth, L. Duranti, J. Rickett, and K. Nihei, 2007, Inverting for reservoir pressure change using time-lapse time strain: Application to genesis field, gulf of mexico: The Leading Edge, **26**, 649–652.

Magesan, M., S. Depagne, K. Nixon, B. Regel, J. Opich, G. Rogers, and T. Hudson, 2005, Seismic processing for time-lapse study: Genesis field, gulf of mexico: The Leading Edge, **24**, 364–373.

Maharramov, M., and B. Biondi, 2014, *in* Joint full-waveform inversion of time-lapse seismic data sets: 954–959.

Routh, P., G. Palacharla, I. Chikichev, and S. Lazaratos, 2012, *in* Full Wavefield Inversion of Time-Lapse Data for Improved Imaging and Reservoir Characterization: 1–6.

Tarantola, A., 1984, in the Acoustic Approximation: **49**, 1259–1266.

Virieux, J., and S. Operto, 2009, An overview of full-waveform inversion in exploration geophysics: Geophysics, **74**, WCC1.